Progress In Electromagnetics Research M, Vol. 116, 11–21, 2023

High-Sensitivity Temperature Sensor Based on Surface Plasmon Resonance Photonic Crystal Fiber

Hai Ping Li, Juan Ruan*, Xin Li, Guang Yong Wei, and Tao He

Abstract—A high-sensitivity photonic crystal fiber (PCF) temperature sensor based on surface plasmon resonance (SPR) with a high figure of merit (FOM) is proposed. Compared with most optical fiber inner air holes coated with metal or placed with metal nanowires, owing to the plasma material directly contacting the analyte, the annular channel outside the cladding is convenient for analyte detection, and the sensor is easier to manufacture. The temperature-sensitive liquid is a mixed solution of ethanol and chloroform with a volume ratio of 1 : 1. The results indicate that the highest sensitivity of this sensor can reach 15.4 nm/°C, and the maximum FOM is 0.2829/°C between −10°C and 60°C. Furthermore, the influence of photonic crystal fiber air hole size, gold film thickness, and other parameters on the performance of the sensor is analyzed.

1. INTRODUCTION

Surface Plasmon Resonance (SPR) is a physical phenomenon of collective oscillation when free electrons in metal interact with the excited electromagnetic field. This phenomenon, due to its high sensitivity, real-time monitoring, and other characteristics, has been widely investigated and applied in Thermal Plasmatics [1–4], Plasma imaging [5, 6], plasmon-enhanced catalysis [7, 8], optical fiber sensing [9, 10], and other fields. The development of semimetals [11–13], semiconductors [14, 15], 2D materials [16, 17], and quantum materials [18, 19] has greatly promoted the development and application of surface plasmon resonance. Ali et al. [20] and West et al. [21] have made pioneering contributions to the field of surface plastics, and these contributions have profoundly influenced modern optics. Jorgensen and Yee proposed and demonstrated the first SPR sensor based on optical fiber in 1993 [22]. The concept of photonic crystal was proposed independently by Yablonovitch [23] and John [24] in 1987. Its unique structure has excellent properties such as high nonlinearity and controllable birefringence characteristics [25, 26], The structure of photonic crystal fiber has a high degree of freedom and can be designed according to requirements. The structure of cladding has a great influence on the propagation mode of photonic crystal fiber, which provides great research space for researchers. However, for photonic crystal fiber, its performance advantage is not high. For example, Li et al. proposed a Sagnac interferometer temperature sensor based on photonic crystal fiber. Its sensitivity is 1.65 nm/°C, and its sensing range is only 25°C ∼ 33°C [27]. To improve the performance of the sensor, PCF and SPR technology are combined to improve the sensing range and sensitivity. For example, Wang et al. proposed a D-type photonic crystal fiber sensor with a sensitivity of 6.36 nm/°C and a sensing range of −5°C–60°C [28]. Han et al. proposed a high-sensitivity temperature sensor based on liquid-filled hollow negative curvature optical fiber surface plasmon resonance. The sensitivity is 2.860 nm/°C, and the temperature sensing range is 20–40°C [29]. To enhance the coupling between SPP mode and core mode and improve the performance of the sensor, the appropriate plasmon resonance material and the appropriate structure of air holes can be selected according to the demand. Gold and silver are commonly used plasma materials. Gold

Received 29 November 2022, Accepted 14 March 2023, Scheduled 27 March 2023
* Corresponding author: Juan Ruan (ruanj2005@163.com).
The authors are with the School of Electronic and Information Engineering, China West Normal University, Nanchong 637009, China.

has good stability and can cause large wavelength drift, while silver resonates more sharply and is easy to oxidize in a humid environment [30], and the thickness of nano-metal film has a great influence on the surface plasmon resonance intensity [31]. The purpose of this paper is to improve the sensitivity of the sensor, and the temperature sensor needs to contact with liquid. Therefore, gold is selected as the plasma material. In addition, in this paper, the air hole and air hole distance of the sensor will be numerically investigated to obtain the best performance of the sensor.

In this paper, an annular polished gold-plated PCF-SPR sensor is proposed. As a plasma material, gold has stability and provides convenience for direct contact with temperature-sensitive liquid. In addition, ethanol and chloroform are placed outside PCF as temperature-sensitive liquids. The effects of air hole diameter, air hole distance, and gold film thickness on the performance of PCF are investigated and optimized by COMSOL software. Finally, by comparing the performance of the sensor, our sensor has superior performance and strong competitiveness in the field of temperature sensors.

2. THE BASIC THEORY OF STRUCTURAL DESIGN

The cross-section of the PCF temperature sensor based on SPR is illustrated in Fig. 1.

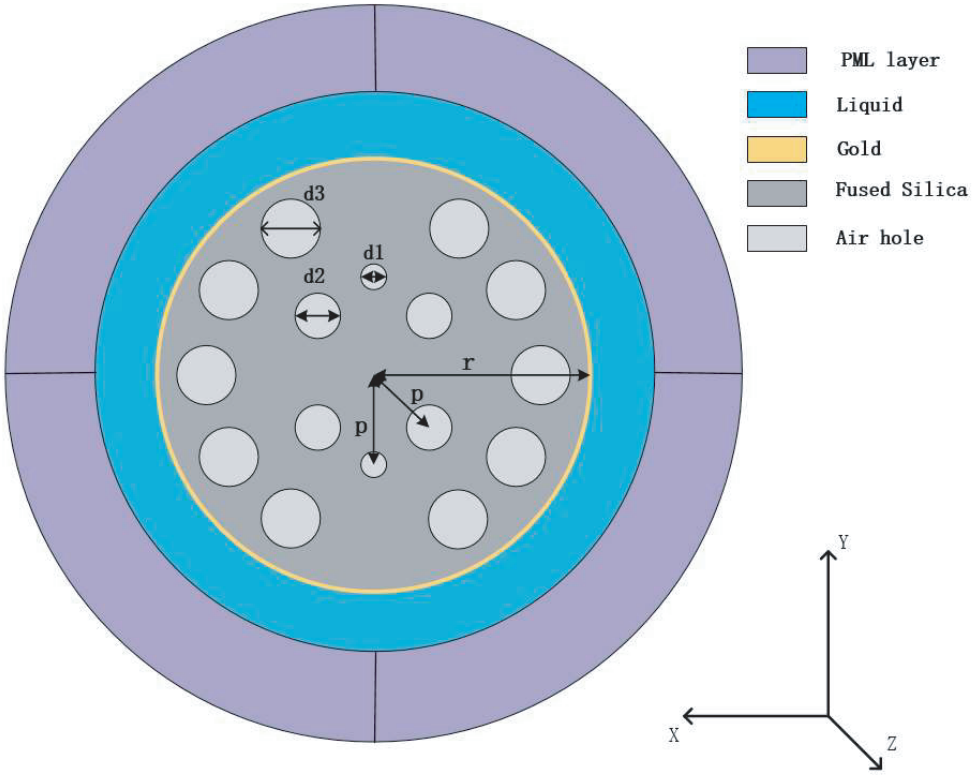

Figure 1. Cross-sectional diagram of PCF-SPR temperature sensor with $d1 = 0.75\,\mu m$, $d2 = 1.5\,\mu m$, $d3 = 1.8\,\mu m$, $r = 6.5\,\mu m$, $t = 37\,nm$, $p = 2.55\,\mu m$.

PCF consists of two layers of air holes, see Fig. 1. The six air holes arranged in a hexagon shape in the inner layer are two small air holes with a diameter of $d1 = 0.75\,\mu m$ and four large air holes with a diameter of $d2 = 1.5\,\mu m$, respectively, which play an important role in adjusting the coupling between the core mode and SPP mode. The outer layer is composed of 10 air holes with a diameter of $d3 = 1.8\,\mu m$. The mode coupling is enhanced by reducing the vertical air holes and the size of the first layer of air holes, and the energy of the core mode is also concentrated. The radius of optical fiber is $r = 6.5\,\mu m$, and a gold nano-coating with a thickness of $t = 37\,nm$ is coated on the cladding after polishing. The temperature-sensitive liquid as the sensing medium is composed of ethanol and

chloroform in a 1 : 1 volume ratio (Chloroform is chosen because of its high thermal sensitivity but high refractive index, so it needs to be mixed with ethanol to reduce its refractive index). The outermost layer is a perfect matching layer with a thickness of 2.6 μm, which is used to absorb the radiant energy and ensure the accuracy of the calculation.

The background material of the PCF-SPR temperature sensor is fused silicon, and its refractive index can be obtained from the Sellmeier equation [32].

$$n^2(\lambda, T) = \left(1.31552 + 6.90754 \times 10^{-6}T\right) + \frac{\left(0.788404 + 23.5835 \times 10^{-6}T\right)\lambda^2}{\lambda^2 - \left(0.0110199 + 0.584758 \times 10^{-6}T\right)} + \frac{\left(0.91316 + 0.548268 \times 10^{-6}T\right)\lambda^2}{\lambda^2 - 100} \quad (1)$$

where the wavelength of incident light λ is in microns, and T is the temperature of centigrade. The temperature range is -10°C to 60°C, but the melting temperature of silicon is 1670°C; therefore, this temperature detection range has little effect on the performance of the optical fiber. The dielectric constant of gold film on the polished surface is analyzed by the Drude-Lorentz model [33]

$$\varepsilon_{Au} = \varepsilon_\infty - \frac{\omega_D^2}{\omega\left(\omega + \mathrm{i}\gamma_D\right)} - \frac{\Delta\varepsilon \cdot \Omega_L}{\left(\omega^2 - \Omega_L^2\right) + \mathrm{i}\Gamma_L\omega} \quad (2)$$

where ε_∞ is the high-frequency dielectric constant of gold; ω is the angular frequency of light; ω_D and γ_D are the plasma frequency and damping frequency, respectively; Ω_L and Γ_L are the frequency and spectral width of Lorentz oscillator, respectively; $\Delta\varepsilon$ is the weight factor. The refractive index of temperature-sensitive liquid [28] can be defined as

$$\begin{aligned} n &= x\% \times [n_{chloroform}|T \\ &= 20^\circ + \frac{\mathrm{dn}_{chloroform}}{dT} \times (T - 20)\Big] + (100 - x)\% \times [n_{ethanol}|T \\ &= 20^\circ + \frac{dn_{ethanol}}{dT} \times (T - 20)\Big] \end{aligned} \quad (3)$$

where $x\%$ and $(100 - x)\%$ represent the ratio of ethanol and chloroform, respectively; dn/dT represents the thermo-optical coefficients of ethanol and chloroform, respectively, and the values are -3.94×10^{-4}/°C and -6.328×10^{-4}/°C, respectively. Ignoring the dispersion of temperature-sensitive liquids, the refractive indices of ethanol and chloroform at $T = 20$°C were assumed to be 1.36048 and 1.43136, respectively. In addition, the ratio of ethanol to chloroform used in this paper is 1 : 1. Because the boiling temperature of ethanol is 78.4°C and that of chloroform is 61.3°C, the upper limit of temperature-sensitive liquid mixed with two substances is 60°C [28].

3. PERFORMANCE ANALYSIS

3.1. Analysis of Electric Field, Dispersion Relation, and Mode Field Loss

The mechanism of the PCF-SPR temperature sensor is expressed as follows: when the incident light propagates in the PCF core in the form of total reflection, the evanescent wave generated by total reflection will act on the free electron oscillation of metal film and excite the surface plasmon wave. When the evanescent wave at a specific wavelength is equal to the wave vector component of the surface plasma wave, the free electrons in the metal film will produce a resonance phenomenon, that is, the SPR phenomenon [34]. This specific wavelength is called phase matching point and resonance wavelength. Therefore, the loss peak will appear at the resonance wavelength. When the temperature changes, the change of temperature to be measured can be obtained by the shift of resonance wavelength.

This paper uses COMSOL simulation software based on the full vector finite element method to simulate the designed sensor under the cooperation of anisotropic PML boundary conditions. The plural form of the effective refractive index of the mode field is

$$n_{eff} = \mathrm{Re}\left(n_{eff}\right) + j\mathrm{Im}\left(n_{eff}\right) \quad (4)$$

Im(*neff*) in the formula is the imaginary part of the effective refractive index, and the confinement loss of mode propagation can be expressed as [35]

$$\alpha = 8.686 \times \frac{2\pi}{\lambda} \times \mathrm{Im}\,(n_{eff}) \times 10^4 \ (\mathrm{dB/cm}) \tag{5}$$

Fig. 2(a) shows the spectral loss diagram of resonance at temperature $T = -10°\mathrm{C}$. It can be concluded that the resonance intensity in the Y polarization direction is far greater than that in the X polarization direction (As marked in black and red solid lines). Therefore, the mode of Y polarization direction is selected to investigate the performance of the sensor in the later calculation. The solid lines marked with point A and point B are the real part of the effective refractive index of surface plasma mode and the real part of core mode respectively (The mode fields corresponding to points A and B are graphs A and B in Fig. 2(b)). In addition, at the resonance wavelength of 1.13 μm, the green solid line intersects with the orange solid line (That is, the effective refractive index real part Re(*neff*) of the two modes coincides). At this wavelength, the core mode transfers the most energy to the SPP mode, and the peak loss is 187.55 dB/cm (The mode field diagram is shown in C diagram in Fig. 2(b), and it can be seen that the resonance intensity is very strong).

Figure 3(a) shows the loss spectra of the Y-pol core mode in the range of $-10°\mathrm{C}$ to $60°\mathrm{C}$. When the temperature changes from $60°\mathrm{C}$ to $-10°\mathrm{C}$, the refractive index of the temperature-sensitive liquid mixture is close to the refractive index of the core mode, so the coupling between the core mode and

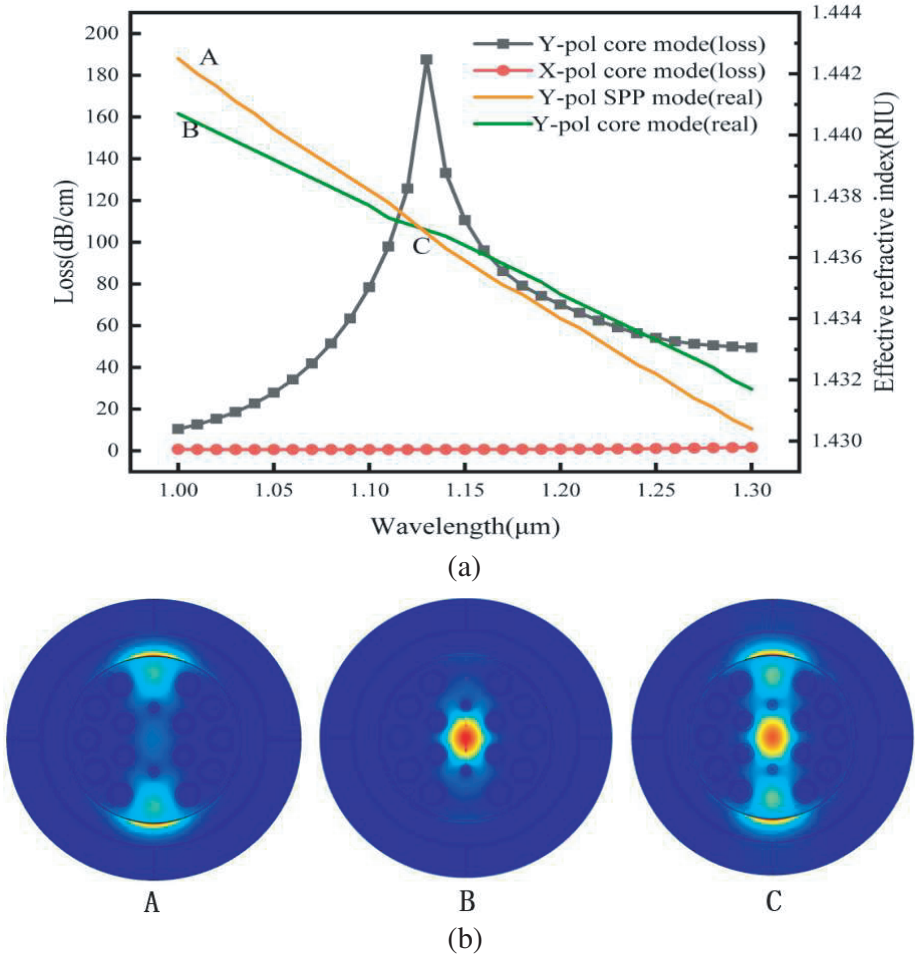

Figure 2. (a) The loss spectra of X-pol (red) and Y-pol (black) core modes and the dispersion relation between Y-pol (green) core mode and SPP (orange) mode at $T = -10°\mathrm{C}$. (b) Distribution of Y-pol electric field.

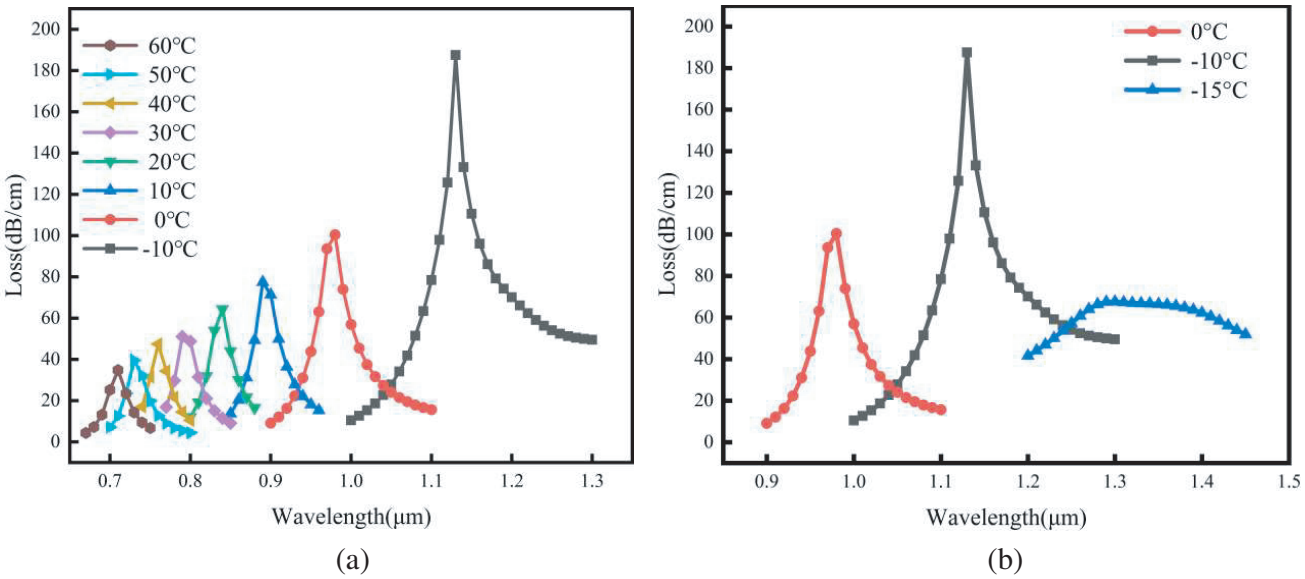

Figure 3. (a) Loss spectra of Y-pol core mode in the temperature range of $-10°$C–$60°$C and (b) from $-15°$C–$0°$C.

SPP mode is enhanced leading to the red shift of the resonance wavelength. At the same time, with the decrease in temperature, the peak loss increases significantly. Fig. 3(b) shows the loss spectra of the Y-pol core mode in the range of $-15°$C to $0°$C. When T is $-10°$C, almost all the energy in the Y-pol core mode is transferred to SPP mode, which reaches complete coupling, and the loss peak drops sharply at the temperature of $-15°$C. Therefore, the lowest temperature reaches up to $-10°$C, and the detection range of this sensor is $-10°$C–$60°$C.

3.2. Optimization of Structural Parameters

When the structural parameters change, the temperature sensing performance will also change. To optimize the performance of the sensor, the influence of inner hole diameters $d1$, $d2$, $d3$, and air hole distance p on the resonant spectrum is systematically studied by changing the studied parameters and keeping other parameters unchanged.

Figures 4(a)–(c) describe the change of loss spectra at temperature $T = -10°$C with different air hole diameters $d1$, $d2$, $d3$, and air hole distance p. The change of air hole will change the phase matching condition, and the resonance wavelength will change. It can be seen that at the same temperature, the diameter of the air hole has little effect on the resonant wavelength, but has a great effect on the peak loss. As illustrated in Fig. 4(a), when the diameter of small circles distributed on the upper and lower sides of the fiber ranges from 0.73 μm to 0.79 μm, with the increase of $d1$, the resonance wavelength experience redshift, and the peak loss first increases and then decreases. The reason for the increase in peak loss is that the core mode and SPP mode are not fully coupled at this time, and the reason for the decrease in peak loss is that the large air hole hinders the energy transfer from the core to the surface plasma material. Fig. 4(b) shows the effect of air hole $d2$ on the loss spectrum. The change of air hole $d2$ has a great effect on the sensing performance because the area of the core is directly changed. If $d2$ is reduced, the loss of the core mode will be reduced, and the coupling will be weakened. If the air hole diameter $d2$ is too large, the core mode will diverge. Fig. 4(c) shows the effect of air hole $d3$ on the loss spectrum. The effect of air hole $d3$ is to reduce the refractive index of the cladding, so the selected air hole diameter is $d3 = 1.8$ μm. Fig. 4(d) shows the influence of air hole distance p on the limited loss spectrum. The appropriate air hole distance plays an important role in the coupling, and the final choice of air hole distance is $p = 2.55$ μm.

Figure 5 shows the confinement loss spectrum of the Au film from 29 nm to 37 nm with an interval

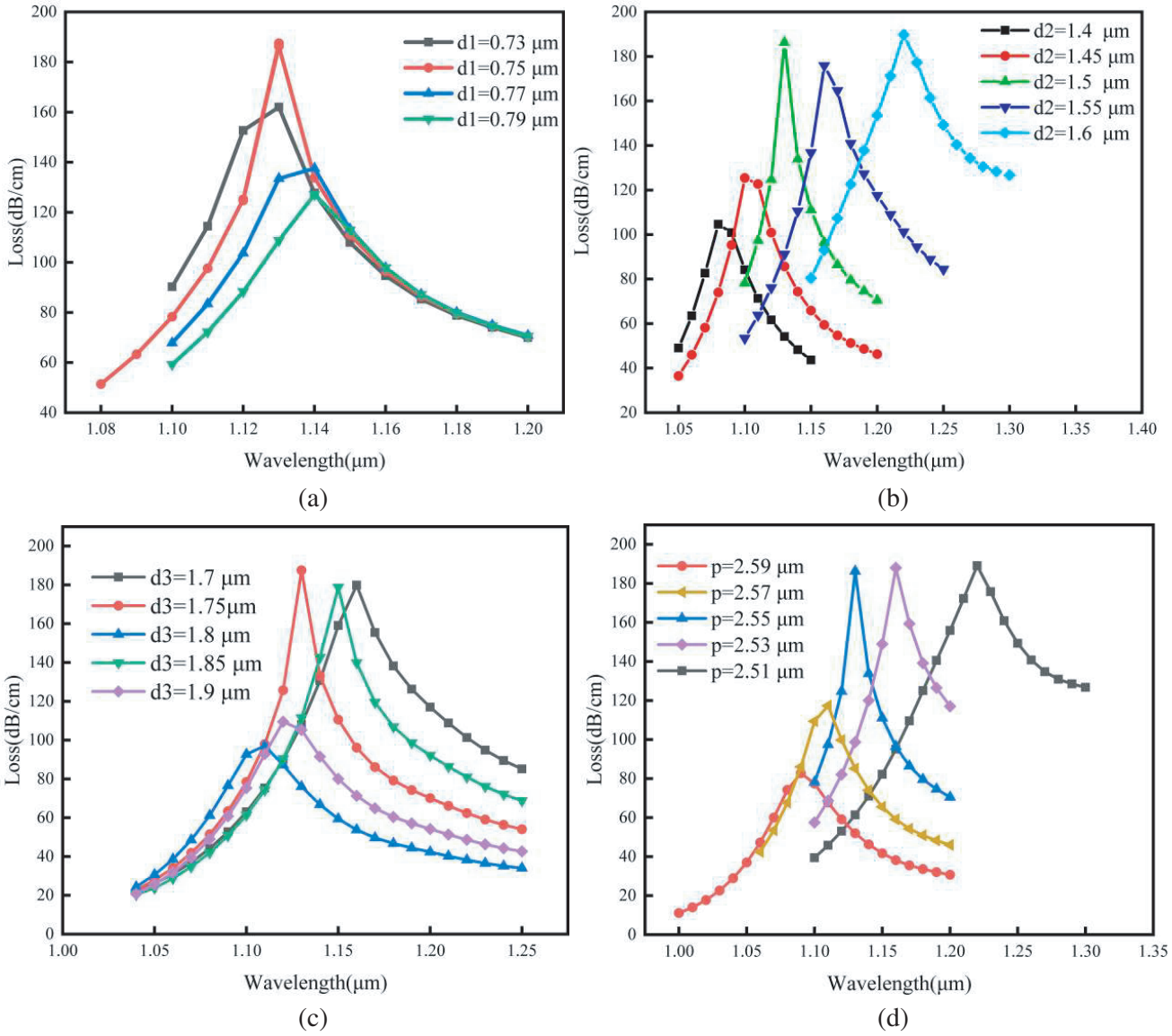

Figure 4. Loss spectra of PCF-SPR sensor under different inner layer hole diameters (a) $d1$, (b) $d2$, (c) $d3$ and (d) different air hole distance p.

of 2 nm at the temperature $T = -10°C$. When the thickness of the gold film increases, the confinement loss increase, and the resonance wavelength has a redshift. When the thickness of the Au film increases from 29 nm to 37 nm, the resonance intensity increases. When $t = 37$ nm, more energy is transferred to the SPP mode, and the highest peak loss is obtained and the narrowest FWHM obtained. Therefore, the optimum choice of the gold film is $t = 37$ nm.

3.3. Analysis of Sensing Performance

The performance of the sensor can be measured by sensitivity, FOM, and linearity between temperature and resonant wavelength. In this paper, the sensitivity of the sensor between −10–60°C is investigated, and its expression is [36]

$$S\,(\mathrm{nm}/^{\circ}\mathrm{C}) = \frac{\Delta\lambda_{peak}}{\Delta T} \tag{6}$$

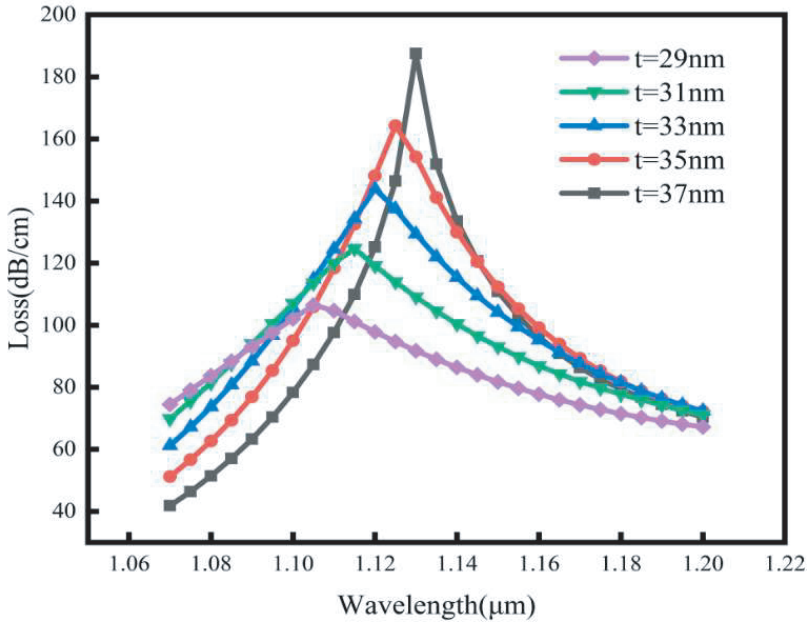

Figure 5. Loss spectra of different gold film thickness.

where $\Delta\lambda_{\text{peak}}$ and ΔT represent the shifting distance of resonance wavelength and change of the temperature, and the sensitivity can be calculated as shown in Table 1. It can be seen from Table 1 that the maximum sensitivity of 15.4 nm/°C can be obtained at −10°C, and the performance is very excellent. In addition, the figure of merit (FOM) of the sensor is another important index to measure the performance of the sensor, and its expression is [37]

$$FOM\,(^{\circ}\text{C}^{-1}) = \frac{S}{FWHM} \tag{7}$$

where S represents sensitivity, FWHM represents full-width at half-maximum, and the maximum FOM of this sensor is 0.2829/°C.

Table 1. Sensing performance of sensors in the range of −10°C–60°C.

T (°C)	λ_{peak} (nm)	$\Delta\lambda_{peak}$ (nm)	S (nm/°C)	FWHM (nm)	FOM ($^{\circ}\text{C}^{-1}$)
−10	1130	154	15.4	54.43	0.2829
0	976	82	8.2	53.34	0.1537
10	894	57	5.7	44.16	0.1291
20	837	43	4.3	38.29	0.1123
30	794	34	3.4	38.99	0.0872
40	760	28	2.8	33.72	0.0830
50	732	23	2.3	33.44	0.0688
60	709			33.13	

Figure 6 shows the fitting results of the cubic equation of loss peak changing with temperature. A good polynomial fitting relationship is obtained between −10°C and 60°C, and the polynomial fitting can reach 0.9965.

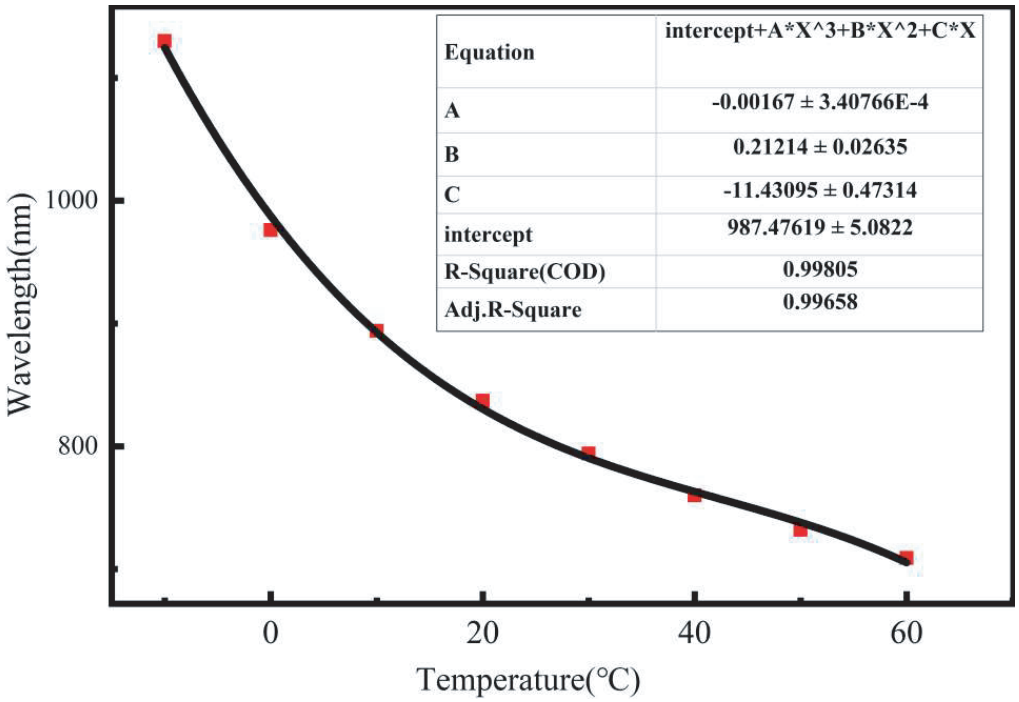

Figure 6. Polynomial fitting diagram of loss peak wavelength changing with temperature.

3.4. Performance Comparison and Experimental Setup

The performance comparison of this work and other schemes is shown in Table 2. It can be seen from the table that this work has great advantages in sensitivity and FOM.

Table 2. Performance comparison of various types of optical fiber sensors.

Structure	Range (°C)	Sensitivity (nm/°C)	FOM	REF
Sagnac interometer	25–33	1.65	-	[27]
D-type PCF-SPR	−5–60	6.36	-	[26]
Liquid-filled PCF-SPR	20–40	2.86	-	[29]
Side-hole filled	20–70	9	-	[38]
Spr	20–80	−2.5	−0.061	[39]
Bandgap-like effect	20–28	−5.5	−0.0762	[40]
This work	−10–60	15.4	0.2829	

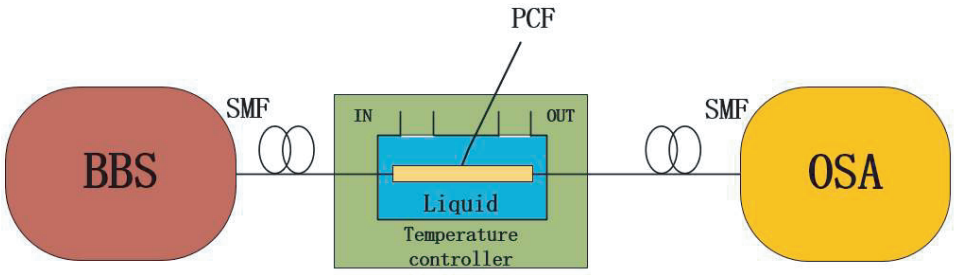

Figure 7. Schematic diagram of PCF-SPR temperature sensor experimental device.

Figure 7 is an experimental device diagram of the temperature sensor. The light source is generated by the broadband light source (BBS), then transfers the PCF-SPR temperature sensor through single-mode fiber, and then transfers the optical spectrum analyzer (OSA) through single-mode fiber. The sensor head is immersed in a thin pipe containing temperature-sensitive liquid. A pump controls the inflow and outflow, and the whole device is placed in a temperature control box. Subsequently, the shift of the resonance wavelength can be observed by an OSA depending on the temperature [41].

4. CONCLUSION

A PCF temperature-sensing structure is proposed. The PCF sensing structure is coated on the surface of optical fiber and can be used for temperature detection. The full vector finite element method is used to simulate and analyze the proposed PCF sensing structure, and the hole diameter, hole distance, and gold film thickness are discussed. The results show that the maximal sensitivity of the sensor can reach 15.4 nm/°C; the temperature sensing range is −10°C–60°C; and the FOM can reach 0.2829/°C. In addition, the sensor is simple in structure and has the advantages of high sensitivity and a wide measuring range.

REFERENCES

1. Politano, A., G. D. Profio, V. Sanna, and E. Curcio, "Thermoplasmonic membrane distillation," *Chemical Engineering Transactions*, Vol. 60, 301–306, 2017.
2. Santoro, S., A. H. Avci, A. Politano, and E. Curcio, "The advent of thermoplasmonic membrane distillation," *Chemical Society Reviews*, Vol. 51, 6087–6125, 2022.
3. Politano, A., G. D. Profio, E. Fontananova, V. Sanna, A. Cupolillo, and E. Curcio, "Overcoming the temperature polarization in membrane distillation by thermoplasmonic effects activated in Ag nanofillers in polymeric membranes," *Desalination*, 192–199, 2019.
4. Abramovich, S., D. Dutta, C. Rizza, S. Santoro, M. Aquino, A. Cupolillo, J. Occhiuzzi, M. F. L. Russa, B. Ghosh, D. Farias, A. Locatelli, D. Boukhvalov, A. Agarwal, E. Curcio, M. B. Sadan, and A. Politano, "NiSe and CoSe topological nodal-line semimetals: A sustainable platform for efficient thermoplasmonics and solar-driven photothermal membrane distillation," *Small*, Vol. 18, No. 31, 2022.
5. Leonardo, V., J. Hu, D. Coquillat, A. Politano, W. Knap, and M. S. Vitiello, "Efficient Terahertz detection in black-phosphorus nano-transistors with selective and controllable plasma-wave, bolometric and thermoelectric response," *Scientific Reports*, 1–10, 2016.
6. [6] Viti, L., D. Coquillat, A. Politano, K. A. Kokh, Z. S. Aliev, M. B. Babanly, O. E. Tereshchenko, W. Knap, E. V. Chulkov, and M. S. Vitiello, "Plasma-wave terahertz detection mediated by topological insulators surface states," *Nanoletters*, Vol. 16, No. 1, 80–87, 2016.
7. Politano, A., G. Chiarello, D. Profio, H. A. Arafat, G. Chiarello, and E. Curcio, "When plasmonics meets membrane technology," *Journal of Physics Condensed Matter*, Vol. 28, No. 36, 2016.
8. Adleman, J. R., D. A. Boyd, D. G. Goodwin, and D. Psaltis, "Heterogenous catalysis mediated by plasmon heating," *Nano Letters*, Vol. 9, No. 12, 4417–4423, 2009.
9. Liu, C., J. Lu, W. Liu, F. Wang, and P. K. Chu, "Overview of refractive index sensors comprising photonic crystal fibers based on the surface plasmon resonance effect," *Chinese Optics Letters*, Vol. 19, No. 10, 102202, 2021.
10. Perri, C., F. Arcadio, G. D'Agostino, N. Cennamo, G. Porto, and L. Zeni, "Chemical and biological applications based on plasmonic optical fiber sensors," *IEEE Instrumentation & Measurement Magazine*, Vol. 24, No. 5, 50–55, 2021.
11. Chiarello, G., J. Hofmann, Z. Li, V. Fabio, L. Guo, X. Chen, and S. D. Sarma, and Antonio Politano, "Tunable surface plasmons in Weyl semimetals TaAs and NbAs," *Physical Review B*, Vol. 99, 121401, 2019.

12. Antonio, P., G. Chiarello, B. Ghosh, K. Sadhkhan, C.-N. Kuo, C. S. Lue, V. Pellegrini, and A. Agarwal, "3D Dirac plasmons in the type-II Dirac semimetal PtTe2," *Physical review letters*, Vol. 121, No. 8, 086804, 2018.
13. Krishanu, S., A. Politano, and A. Agarwal, "Novel undamped gapless plasmon mode in a tilted type-llDirac semimetal," *Physical Review Letters*, Vol. 124. No. 4, 2020.
14. Antonio, P., L. Viti, and M. Vitiello, "Optoelectronic devices, plasmonics, and photonics with topological insulators," *APL Materials*, Vol. 5, No. 3, 2017.
15. Amit, A., M. S. Vitiello, L. Viti, A. Cupolillo, and A. Politano, "Plasmonics with two-dimensional semiconductors: From basic research to technological applications," *Nanoscale*, Vol. 10, No. 19, 8938–8946, 2018.
16. Antonio, P. and G. Chiarello, "Quenching of plasmons modes in air-exposed graphene-Ru contacts for plasmonic devices," *Applied Physics Letters*, Vol. 102, No. 20, 2013.
17. Cupolillo, A., A. Politano, N. Ligato, D. M. CidPerez, G. Chiarello, and L. S. Caputi, "Substrate-dependent plasmonic properties of supported graphene," *Surface Science*, 76–80, 2015.
18. Debasis, D., B. Ghosh, B. Singh, H. Lin, A. Politano, A. Bansil, and A. Agarwal, "Collective plasmonic modes in the chiral multifold fermionic material CoSi," *Physical Review B*, Vol. 105, No. 16, 2022.
19. Antonio, P., V. M. Silkin, I. A. Nechaev, M. S. Vitiello, L. Viti, Z. S. Aliev, M. B. Babanly, G. Chiarello, P. M .Echenique, and E. V. Chulkov, "Interplay of surface and Dirac plasmons in topological insulators: the case of Bi2Se3," *Physical Review Letters*, Vol. 115, No. 21, 2015.
20. Ali, S., A. Lauchner, S. Najmaei, C. A. Orozco, FF. Wen, J. Lou, and N. Halas, "Enhancing the photocurrent and photoluminescence of single crystal monolayer MoS2 with resonant plasmonic nanoshells," *Applied Physics Letters*, Vol. 104, No. 3, 2014.
21. West, P. R., S. Lshii, G. V. Naik, N. K. Emani, V. M. Shalaev, and A. Boltasseva, "Searching for better plasmonic materials," *Laser & Photonics Reviews*, Vol. 4, No. 6, 795–808, 2010.
22. Jorgenson, R. C. and S. S. Yee, "A fiber-optic chemical sensor based on surface plasmon resonance," *Sensors and Actuators B: Chemical*, Vol. 12, No. 3, 213–220, 1993.
23. Yablonovitch, E., "Inhibited spontaneous emission in solid-state physics and electronics," *Physical Review Letters*, Vol. 58, No. 20, 2059–2062, 1987.
24. John, S., "Strong localization of photons in certain disordered dielectric superlattices," *Physical Review Letters*, Vol. 58, No. 23, 2486–2489, 1987
25. Otupiri, R., E. K. Akowuah, and S. Haxha, "Multi-channel SPR biosensor based on PCF for multi-analyte sensing applications," *Optics Express*, Vol. 23, No. 12, 15716, 2015.
26. Xue, J., S. Li, Y. Xiao, W. Qin, X. Xin, and X. Zhu, "Polarization filter characters of the gold-coated and the liquid-filled photonic crystal fiber based on surface plasmon resonance," *Optics Express*, Vol. 21, No. 11, 13733, 2013.
27. Li, X.-G., Y. Zhao, X. Zhou, and L. Cai, "High sensitivity all-fiber Sagnac interferometer temperature sensor using a selective ethanol-filled photonic crystal fiber," *Instrumentation Science & Technology*, Vol. 46, No. 3, 253–264, 2017.
28. Wang, S., Y. Lu, W. Ma, N. Liu, and S. Fan, "D-shaped surface plasmon photonic crystal fiber temperature sensor," *Plasmonics*, 1–9, 2022.
29. Han, Y., L. Gong, F. Meng, H. Chen, Y. Wang, Z. R. Li, F. D. Zhou, M. Yang, J. Z. Guan, W. Yun, X. J. Guo, and W. Wang, "Highly sensitive temperature sensor based on surface plasmon resonance in a liquid-filled hollow-core negative-curvature fiber," *Optik*, Vol. 241, 2021.
30. Rifat, A., G. Mahdiraji, D. Chow, Y. Shee, R. Ahmed, and F. Adikan, "Photonic crystal fiber-based surface plasmon resonance sensor with selective analyte channels and graphene-silver deposited core," *Sensors*, Vol. 15, No. 5, 11499–11510, 2015.
31. Antonio, P. and G. Chiarello, "The influence of electron confinement, quantum size effects, and film morphology on the dispersion and the damping of plasmonic modes in Ag and Au thin films," *Progress in Surface Science*, Vol. 90, No. 2, 144–193, 2015

32. Ghosh, G., M. Endo, and T. Iwasaki, "Temperature-dependent Sellmeier coefficients and chromatic dispersions for some optical fiber glasses," *Journal of Lightwave Technology*, Vol. 12, No. 8, 1338–1342, 1994.
33. Vial, A., A.-S. Grimault, D. Macías, D. Barchiesi, and M. L. Chapelle, "Improved analytical fit of gold dispersion: Application to the modeling of extinction spectra with a finite-difference time-domain method," *Physical Review B*, Vol. 71, No. 8, 2005.
34. Yan, X., R. Fu, T. Cheng, and S. Li, "A highly sensitive refractive index sensor based on a V-shaped photonic crystal fiber with a high refractive index range," *Sensors*, Vol. 21, 3782, 2021
35. Rifat, A. A., G. A. Mahdiraji, Y. M. Sua, Y. G. Shee, R. Ahmed, D. M. Chow, and F. R. M. Adikan, "Surface plasmon resonance photonic crystal fiber biosensor: A practical sensing approach," *IEEE Photonics Technology Letters*, Vol. 27, No. 15, 1628–1631, 2015.
36. Danlard, I. and E. K. Akowuah, "Assaying with PCF-based SPR refractive index biosensors: From recent configurations to outstanding detection limits," *Optical Fiber Technology*, Vol. 54, 102083, 2020.
37. Lou, J., TL. Cheng, S. G. Li, and X. N. Zhang, "Surface plasmon resonance photonic crystal fiber biosensor based on gold-graphene layers," *Optical Fiber Technology*, Vol. 50, 206–211, 2019.
38. Reyes Vera, E., C. M. Cordeiro, and P. Torres, "Highly sensitive temperature sensor using a Sagnac loop interferometer based on a side-hole photonic crystal fiber filled with metal," *Applied Optics*, Vol. 56, No. 2, 156–162, 2017.
39. Liu, Q., S. G. Li, H. L. Chen, Z. K. Fan, and J. S. Li, "Photonic crystal fiber temperature sensor based on coupling between liquid-core mode and defect mode," *IEEE Photonics Journal*, Vol. 7, No. 2, 1–9, 2015.
40. Mo, X., J. T. Lv, Q. Liu, X. X. Jiang, and G. Y. Si, "A magnetic field SPR sensor based on temperature self-reference," *Sensors* Vol. 21, No. 18, 6130, 2021.
41. Rifat, A. A., R. Ahmed, G. A. Mahdiraji, and F. R. M. Adikan, "Highly sensitive D-shaped photonic crystal fiber-based plasmonic biosensor in visible to near-IR," *IEEE Sensors Journal*, Vol. 17, No. 9, 2776–2783, 2017.